

Metastable γ -Li₂TiTeO₆: Negative Chemical Pressure Interception and Polymorph Tuning of SHG

Mei-Huan Zhao, Xiao Zhou, Yifeng Han, Dequan Jiang, Yonggang Wang,* Kuo Li, Haiyan Zheng, Huiyang Gou, Ling Chen, and Man-Rong Li* **HPSTAR**
1600-2022



Cite This: *Chem. Mater.* 2022, 34, 10153–10161



Read Online

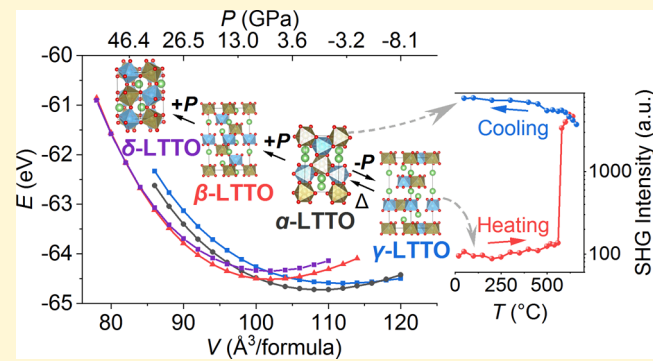
ACCESS |

Metrics & More

Article Recommendations

Supporting Information

ABSTRACT: Intercepting metastable phases by chemical approaches is an important solution to explore structural varieties of functional materials under positive/negative pressure, as paradigmatically exemplified by the polymorph modification in Li₂TiTeO₆. Here, we stabilized a novel metastable Li₂TiTeO₆ (denoted as γ -phase) in the ordered-ilmenite-type R3 via facile topotactic reaction from Na₂TiTeO₆, which was found to crystallize in R3 instead of the reported R̄ structure. The calculated equilibrium volume of γ -Li₂TiTeO₆ is larger than that of the ground-state *Pmn2*-Li₂TiTeO₆ (denoted as α -phase), indicating that γ -Li₂TiTeO₆ can only be stabilized under “negative pressure” quantified to be around -6 GPa. The γ -phase irreversibly transforms into the α -phase around 560 °C under ambient pressure, accompanied by a steep increase (~500 times) of the second harmonic generation (SHG), indicating a potential application of γ -Li₂TiTeO₆ as an optical thermometer. These findings elegantly show that chemical pressure as well as physical pressure is powerful to tune the polymorphs for metastable phases and exotic properties as paradigmatically exemplified by Li₂TiTeO₆, which undergoes consecutive polymorph tuning of γ (-6 GPa), α (0 GPa), β (6 GPa, R3-Ni₃TeO₆ type), and δ (40 GPa, predicted *P21/n* double perovskite) phases with densified atomic packing.



There are four commonly used chemical approaches (Figure 1) to stabilize metastable polymorphs, including solid-solution (bulk trapping, Figure 1a),^{8–10} topotactic reaction (ionic exchange, Figure 1b),^{11–13} interfacial strain (epitaxial growth, Figure 1c),^{14–16} and nanoparticles (surface energy effect, Figure 1d). (a) Solid-solution strategy is effective to trap metastable phases in the (locally) isostructural matrix and tune the physical properties by modulating the ionic ordering degree, where the lattice mismatch between the host and guest phases evokes volumetric compression/expansion to capture the metastable phases.^{8,21,22} (b) Topotactic ion exchange is a chemical approach that replaces cations, anions, or ionic groups with new ones under relatively mild conditions, without breaking the original structure frameworks. This approach is

INTRODUCTION

It is common sense that structures decide properties. Therefore, it is important to seek more polymorphs for a given chemical formula and discover more exotic physical properties.¹ High-temperature solid-state reaction is a conventional and important way for synthesizing functional materials, which however usually produces only thermodynamically stable phases and skips the intriguing metastable phases. As shown in Figure 1, high-pressure and high-temperature synthesis is one of the effective ways to obtain metastable polymorphs with higher density (smaller cell volume per formula unit).^{2–4} For instance, metastable Na₃Cl and NaCl₃ with novel stoichiometries are obtained by compressing NaCl and excess sodium or chloride up to 80 GPa.⁵ Nonpolar C2/m CuNbO₃ transforms to a metastable ferrielectric perovskite-type structure upon quenching at 1273 K under 12 GPa.⁶ However, on one hand, high-pressure synthesis may ignore the metastable phases with larger volumes (lower density) than those of the relatively stable ones, since physically, high pressure mostly causes compressing effect (volume contraction). On the other hand, some metastable phases may be unquenchable from high pressure to ambient pressure. Moreover, high-pressure experiments are of high cost and low yield, making it hard to realize large-batch production for

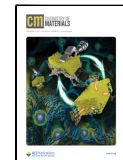
applications. Therefore, it is important to intercept metastable phases using the more feasible chemical ways (chemical pressure).⁷

There are four commonly used chemical approaches (Figure 1) to stabilize metastable polymorphs, including solid-solution (bulk trapping, Figure 1a),^{8–10} topotactic reaction (ionic exchange, Figure 1b),^{11–13} interfacial strain (epitaxial growth, Figure 1c),^{14–16} and nanoparticles (surface energy effect, Figure 1d). (a) Solid-solution strategy is effective to trap metastable phases in the (locally) isostructural matrix and tune the physical properties by modulating the ionic ordering degree, where the lattice mismatch between the host and guest phases evokes volumetric compression/expansion to capture the metastable phases.^{8,21,22} (b) Topotactic ion exchange is a chemical approach that replaces cations, anions, or ionic groups with new ones under relatively mild conditions, without breaking the original structure frameworks. This approach is

Received: September 27, 2022

Revised: October 28, 2022

Published: November 7, 2022



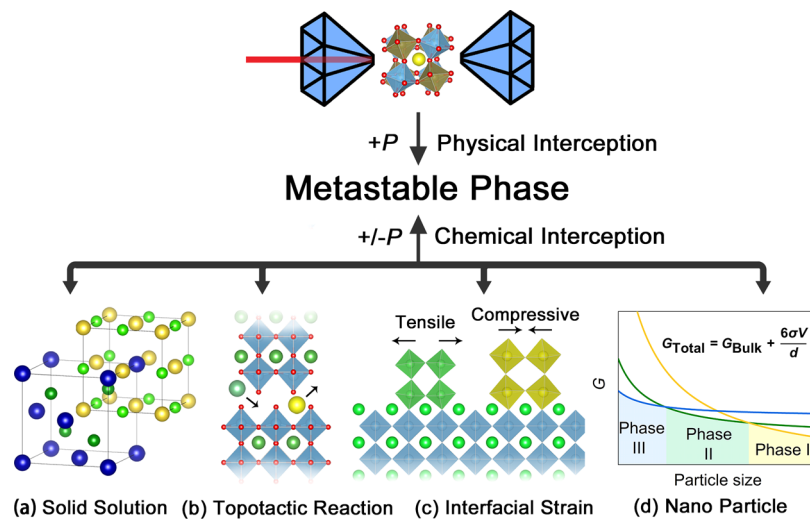


Figure 1. Physical and chemical schemes to intercept metastable phases. There are four ways of chemical interception, namely, (a) solid solution, (b) topotactic interception, (c) interfacial strain, and (d) nanoparticle. The inset formula in (d) means the total Gibbs free energy (G_{Total}) is composed of bulk (G_{Bulk}) and surface energy ($\frac{6\sigma V}{d}$, where σ , V , and d represent specific surface energy, volume, and particle size, respectively). Phases I–III successively become the most stable phase as particle size decreases.

usually applied for pseudo-two-dimensional (2D) or one-dimensional (1D) materials because of their low energy barriers of ionic migration, except for $\text{Ni}_{0.5}\text{TaO}_3$ ²³ and $\text{Li}_{0.1}\text{Fe}_{0.45}\text{NbWO}_6$ ²⁴ the only two reported topotactic products from three-dimensional (3D) close-packed precursors. 3D and quasi-2D perovskite derivatives, such as the Ruddlesden–Popper, Dion–Jacobson, and Aurivillius type phases, could transform into one another by manipulating ion-exchange reactions.^{25–29} LiSbO_3 , which derives the structure of $Pnn2$ – $\text{Li}_2\text{TiTeO}_6$ (LTTO, hereafter denoted as the α -phase) with ordering the Sb^{5+} site to two alternatively arranged cations, can transform to a denser LiNbO_3 -type phase at 7.7 GPa and adopt a less dense ilmenite-like monoclinic phase (with slight gliding of SbO_6 octahedron layers) by the topotactic reaction.^{30,31} Here, ion exchange is successful in obtaining metastable phases only existing under “negative pressure” (cell expansion). (c) Epitaxial growth of metastable structures can be realized by interfacial lattice mismatch between the epitaxy and substrate.³² The polar polymorph of ScFeO_3 prepared at 6 GPa in bulk has been successfully stabilized at ambient pressure on the SrRuO_3 / SrTiO_3 substrate.³³ Some composite thin films are exposed to in-plane and out-of-plane strains from heterogeneous surfaces at the same time, and the metastable phases are hence stabilized in three dimensions.^{15,34} (d) Nanomaterials possess a large specific surface area compared to their bulk analogues. At the nanoscale, the surface energy ($6\sigma V/d$, σ , V , and d are specific surface energy, volume, and particle size, respectively) plays a critical role in the total energy (G_{Total}) so that it may overcome the energy difference between stable (G_{Bulk}) and metastable phases and thus stabilize the metastable phases in nanoscale at ambient pressure.^{35,36} For instance, α - Fe_2O_3 can subsequently transform to metastable β - Fe_2O_3 (50 nm), ϵ - Fe_2O_3 (30 nm), and γ - Fe_2O_3 (8 nm) as the particle size decreases.¹⁹ All these chemical interception routes have their unique features suitable for different applications and are widely applied to exploit metastable phases. Among all of the above-mentioned approaches, topotactic ion exchange is the most facile route for scaled-up yield and practical applications.

In this work, we take LTTO as an example, to paradigmatically illuminate the function enhancement by polymorph engineering via positive physical pressure (hydraulic pressure) and negative chemical pressure (topotactic reaction). LTTO was found to transform from stable $Pnn2$ (α) to metastable Ni_3TeO_6 (NTO)-type $R3$ (β) under high pressure (6 GPa) upon temperature quenching as predicted.³⁷ Given the similar chemical compositions and local structure between β -LTTO and $\text{Na}_2\text{TiTeO}_6$ (NTTO), it is thus expected to obtain a metastable LTTO phase via the topotactic reaction. Here, we revisited the structure of NTTO and found out that NTTO adopts the ordered-ilmenite (OIL)-type $R3$ structure rather than the reported ilmenite ($\overline{R3}$) symmetry. A new OIL-type metastable γ -LTTO was obtained by low-temperature topotactic ion exchange from NTTO. The crystal structure, thermal stability, and physical properties of this γ -phase were extensively studied, which went through a first-order phase transition to the α -analogue when heated up to 560 °C at atmospheric pressure, accompanied by an irreversible and intensive increase of the second harmonic generation (SHG) intensity by about 500 times. A much denser $P21/n$ perovskite polymorph of LTTO (denoted as the δ -LTTO) was also predicted around 40 GPa. Here, we denote the ambient pressure phase ($Pnn2$), high-pressure phase (NTO-R3), topotactic exchange phase (OIL-R3), and predicted monoclinic structure of LTTO by α -, β -, γ -, and δ -LTTO, respectively, for convenient discussion.

■ EXPERIMENTS AND METHODS

Polycrystalline NTTO was synthesized by a conventional solid-state reaction using stoichiometric Na_2CO_3 (99.99%, Aladdin), TiO_2 (rutile, 99.99%, Macklin), and TeO_2 (99.99%, Aladdin) according to the literature.³⁸ The raw material mixture was homogeneously ground and heated up to 600 °C for 12 h to completely oxidize Te^{4+} to Te^{6+} . The precalcined powder was ground again for a homogeneous distribution before being heated at 700 °C for 12 h to obtain NTTO. The as-made NTTO precursor was mixed with LiNO_3 (99.99%, Aladdin) at the molar ratio of 1:10 with fine grinding. The mixture was reacted at 400 °C (heating rate of 5 °C/min) for 24 h for a thorough exchange of Na^+ with Li^+ to form LTTO,

followed by natural cooling. The resulting products were washed with pure water and then centrifuged to remove excess LiNO_3 and the byproduct NaNO_3 before being dried at 70 °C in the atmosphere.

The phase purity and crystal structure of NTTO were characterized by powder X-ray diffraction (PXD) using Empyrean PANalytical equipped with a Cu target ($\lambda = 1.5418 \text{ \AA}$). The phase and structure information of LTTO were examined by synchrotron powder X-ray diffraction (SPXD) on the beamline BL14B at Shanghai Synchrotron Radiation Facility (SSRF) with a wavelength of 0.68993 \AA . The in situ variant-temperature PXD of LTTO was measured by a Rigaku SmartLab diffractometer equipped with a Cu target ($\lambda = 1.5418 \text{ \AA}$). The diffraction data were refined with the Rietveld method using the TOPAS software package.³⁹ The powder SHG measurements were performed by a homemade optical system equipped with an exciting light source of fiber laser (NPI LASER Co., Ltd, 1064 nm, 20 MHz, 15 ps), for which the powder samples were sieved to obtain grain size ranging from 25 to 45 μm . As for temperature-dependent SHG measurements (Figure S1), the powder sample was placed in the Al_2O_3 sample holder and heated inside a circular column-like furnace. The temperature is determined by a thermocouple close to the sample. The laser produces incident light of 1064 nm. The emission light of doubled frequency, 532 nm, is detected by a photomultiplier tube. The charge-coupled device (CCD) is for observing the sample and focusing. The elemental analyses of LTTO and NTTO were performed by an energy-dispersive spectrometer (EDS) equipped with a scanning electron microscope (SEM, GeminiSEM500 and JSM 7900F). The differential scanning calorimetry (DSC) measurements were performed with a NETZSCH DSC 404F3 instrument.

The internal energy–volume ($E-V$) curves of LTTO and NTTO were computed with density functional theory (DFT) using the Vienna *Ab initio* Simulation Package (VASP)⁴⁰ to evaluate the pressure-dependent phase evolution. The structural relaxations were carried out using generalized gradient approximation (GGA) implemented in the Perdew–Burke–Ernzerhof (PBE) method⁴¹ as the exchange-correlation function until the forces converge to 0.01 eV/ \AA . The plane-wave basis set was employed with a cutoff energy of 700 eV. A Γ -centered k -point grid of $9 \times 9 \times 9$ was used for sampling in the Brillouin zone. For γ -LTTO, Ti and Te are highly disordered in two 3a Wyckoff sites. To realize structural optimization for γ -LTTO and NTTO using DFT, Ti and Te were set to individually occupy the two 3a sites in the initial structure models for calculations, which did not break the symmetry of the OIL-type structure. The obtained $E-V$ curves were fitted with the Murnaghan equation of state (EOS)⁴² to calculate the equilibrium volume (V_0) for each LTTO polymorph.

■ RESULTS AND DISCUSSION

Structural Characterization of NTTO and LTTO.

NTTO is a high dielectric material that has been reported to adopt the ilmenite-type $R\bar{3}$ structure and transform to a $P21/n$ perovskite-type phase after high-pressure and high-temperature treatment at 7 GPa and 950 °C.³⁸ In this study, we reinvestigated the structure of the NTTO precursor to fully understand the structure of γ -LTTO, the topotactic exchange product of NTTO. The as-obtained NTTO precursor was first confirmed to be pure with stoichiometric ingredient by laboratory PXD (Figures 2a and S2a in the Supporting Information) and EDS (Figure S3a) measurements, giving nominal formula of $\text{Na}_2\text{Ti}_{0.99(1)}\text{Te}_{1.00(1)}\text{O}_6$. Therefore, the molar ratio of Ti and Te was constrained to be 1:1 during the subsequent structural refinements. As shown in Figure 2c, the SHG intensity of NTTO is proportional to the square of incident light power and comparable to that of KH_2PO_4 (KDP), which indicates the SHG activity and noncentrosymmetry of NTTO. These findings corroborate that the reported $R\bar{3}$ structural model of NTTO is improper,³⁸ although the goodness of fittings seems reasonable (Figure S4 and Table S1). Accordingly, the actual noncentrosymmetric structure of

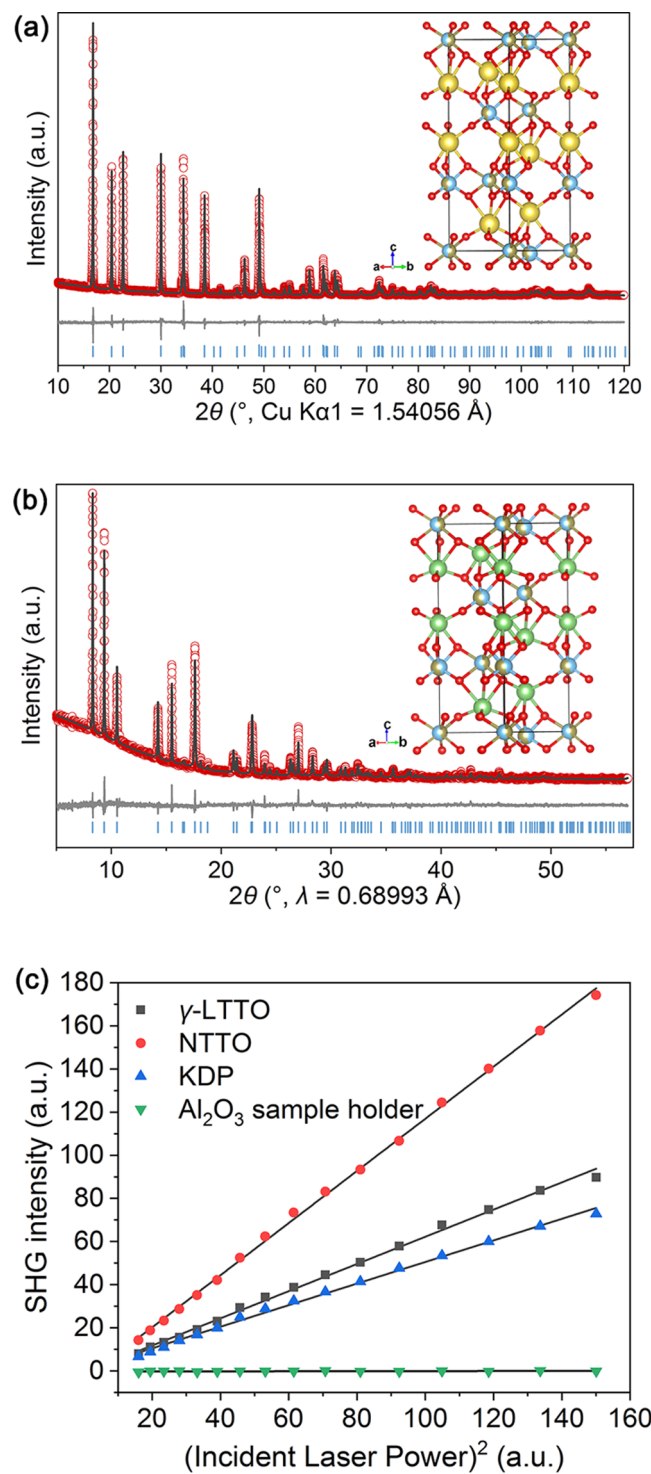


Figure 2. Rietveld refinement results of (a) NTTO and (b) γ -LTTO. The red circles, black lines, gray lines, and blue ticks are the observed, calculated, difference, and index signals, respectively. The insets are the crystal structures of NTTO and γ -LTTO in (a) and (b), respectively. The spheres in green, yellow, blue, brown, and red represent Li^+ , Na^+ , Ti^{4+} , Te^{6+} , and O^{2-} , respectively. (c) Comparison of the SHG intensities of γ -LTTO, NTTO, KDP, and the blank sample holder versus the squares of incident laser power.

NTTO should be similar in atomic coordinates to the $R\bar{3}$ structure, which prompted us to resort to the OIL-type $R\bar{3}$ structure.⁴³ The decent refined results are shown in Figure 2a and Table S1. The obtained acentric structure has the same

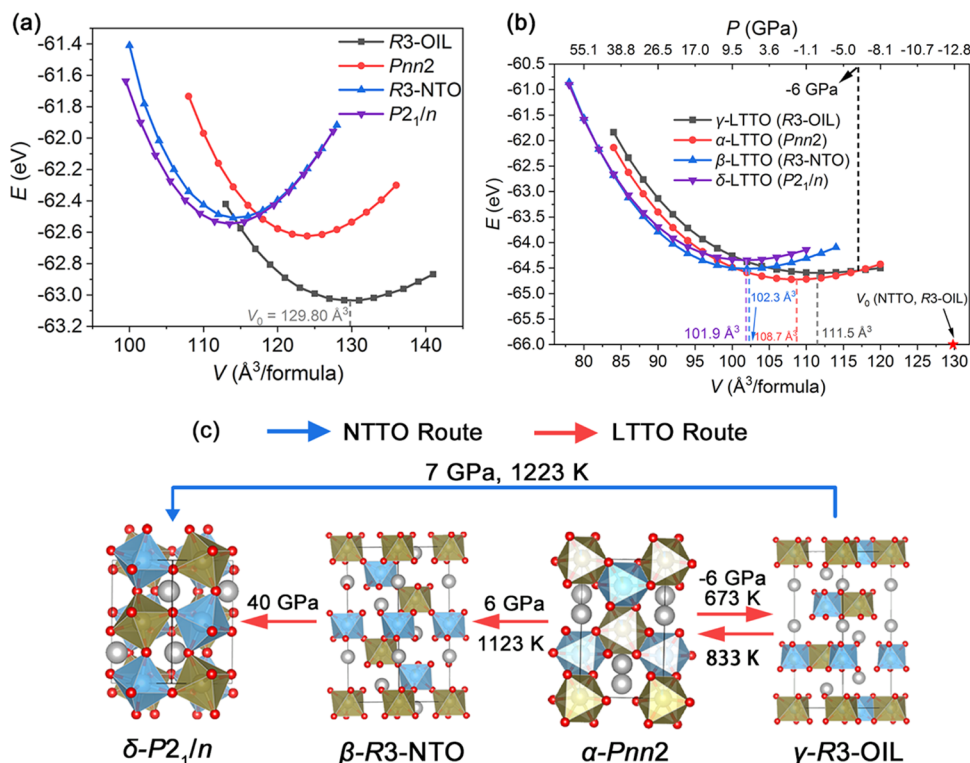


Figure 3. (a) E – V curves of NTTO in R3-OIL (black line), $Pnn2$ (red line), R3-NTO (blue line), and $P2_1/n$ (purple line). (b) E – V curves of γ -LTTO (black line), α -LTTO (red line), β -LTTO (blue line), and δ -LTTO (purple line). The equilibrium volumes are pointed out by the dotted lines with the corresponding colors, and the values of V_0 are labeled with the same color. The top axis demonstrates the P – V relation referenced to α -LTTO. The red star symbol in (b) repeats the equilibrium volume of NTTO in R3-OIL for clear comparison. (c) Schematic phase transition flows of NTTO (blue arrows) and LTTO (red arrows).

cell dimension as that of the originally proposed $\bar{R}\bar{3}$, giving $a = 5.21725(4)$ Å and $c = 15.8262(2)$ Å. In this OIL-type NTTO, the honeycomb-like layers are composed of edge-sharing LiO_6 octahedra alternatively stacking with those built by $(\text{Ti}/\text{Te})\text{O}_6$ octahedra along the c -axis, as the motifs observed in $\text{Li}_2\text{GeTeO}_6$,⁴⁴ $\beta\text{-Mn}_2\text{InSbO}_6$,⁴⁵ $\text{Mn}_2\text{LiReO}_6$,⁴⁶ and $\text{Mn}_2\text{FeMoO}_6$.⁴⁷ Structurally, the atomic coordinates of 3a and 9b sites in $R\bar{3}$ are equivalent to those of 6c and 18f sites in $\bar{R}\bar{3}$, respectively, within the accuracy of the Rietveld refinements as shown in the insets of Figures 2a and S4, which implies that the atomic coordinates of NTTO in $R\bar{3}$ still comply with those of the $\bar{R}\bar{3}$ symmetry. Nevertheless, Ti and Te are homogeneously and randomly distributed throughout the reported $\bar{R}\bar{3}$ structure. In contrast, the Ti/Te occupancies are unequal in the two 3a sites in the OIL structure, which results in the absence of an inversion center and well explains the presence of SHG activity in Figure 2c. As a result, NTTO conclusively adopts the OIL-type $R\bar{3}$ structure with a Ti/Te ordering degree of 8% (occupancy of 0.540(16)/0.460(16)) rather than the reported ilmenite-type $\bar{R}\bar{3}$ structure. We also calculated the E – V curves of the OIL-type and $P2_1/n$ NTTO along with the $Pnn2$ and NTO-type structures reported for LTTO. As shown in Figure 3a, with volume contraction, the energy of the OIL-type structure becomes higher than that of the $P2_1/n$ structure in NTTO, while the energy of $Pnn2$ and NTO-type structures are too high for them to be driven by high pressure. The calculation results of different NTTO polymorphs predict the OIL to $P2_1/n$ transformation under high pressure, which is in good agreement with the experimental discovery,³⁸ and further verify the ambient structure of NTTO to be OIL- $R\bar{3}$ rather than the ilmenite $\bar{R}\bar{3}$.

γ -LTTO is the topotactic ion-exchange product of NTTO, thus it is expected to inherit the structural framework of NTTO with Na^+ replaced by Li^+ . PXD measurements proved the purity and cell dimension of the as-made γ -LTTO (Figure S2b). Elemental analysis by EDS confirms the thorough replacement of Na^+ by Li^+ and gives a nominal formula of $\text{Li}_2\text{Ti}_{0.95(1)}\text{Te}_{1.00(1)}\text{O}_6$ as shown in Figure S3b. The SHG activity of γ -LTTO in Figure 2c further corroborates its acentric structure nature. Thereby, the SPXD data were refined in the OIL-type $R\bar{3}$ structural model. The overall molar ratio of Ti and Te was restricted to 1:1 according to the EDS results. The refinement results and crystallographic details are shown in Figure 2b and Table S2. The refined OIL structure gives $a = 5.11601(4)$ Å, $c = 14.30863(19)$ Å, and $V = 324.333(7)$ Å³. The Ti/Te ordering degree in γ -LTTO is 13% (occupancy of 0.562(19)/0.438(19)). The unit cell volume of γ -LTTO is 13.06% smaller than that of the NTTO precursor (373.068(8) Å³) due to the ionic radius difference between Na^+ (1.02 Å, sixfold coordination) and Li^+ (0.76, sixfold coordination).⁴⁸ The crystal structure of this topotactic γ -LTTO phase is shown in the inset of Figure 2b, which is isostructural to the OIL-type NTTO but with a slightly different cationic ordering degree.

Universal Pressure-Dependent Polymorph Modulation. Seven polymorphs are known for the exotic perovskite-related $A_2\text{BB}'\text{O}_6$ compounds, among which Li_2BTeO_6 are more likely to crystallize in R3-OIL, $Pnn2$, R3-NTO, and $P2_1/n$ structures.³⁷ Here, the E – V curves for the above four possible polymorphs were computed for LTTO using DFT, as shown in Figure 3b, where the α -phase ($Pnn2$) is the most stable one with the lowest internal energy at V_0 (ambient pressure), docking on the energy convex hull of the phase diagram

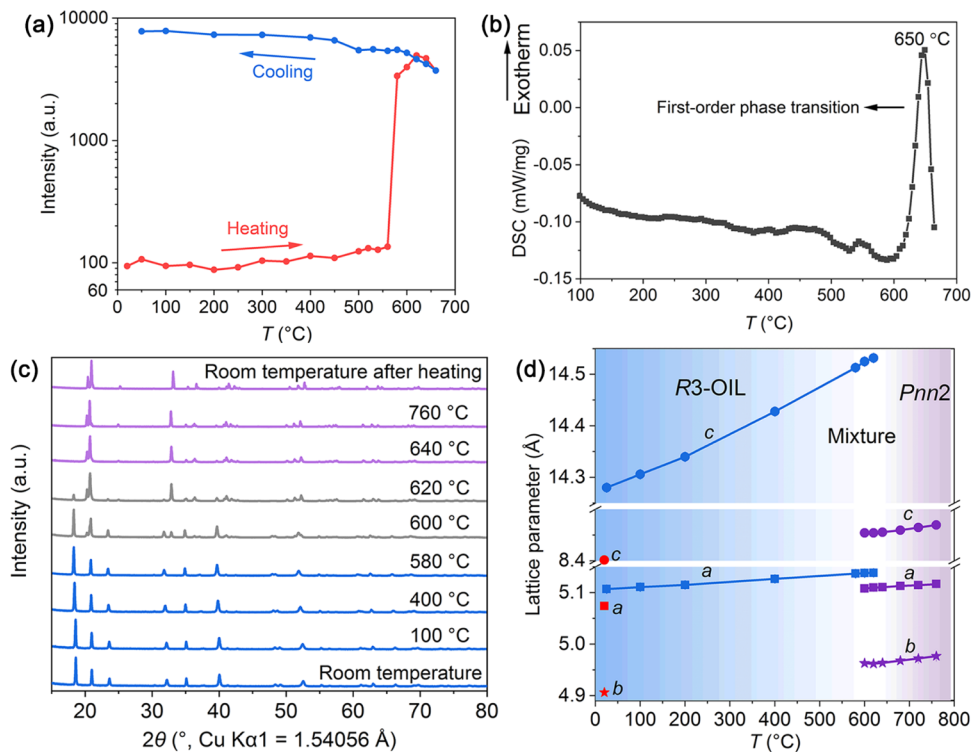


Figure 4. (a) In situ temperature-dependent SHG intensity of γ -LTTO. The red solid line represents the intensities up to 680 °C before decomposition, after which the sample was cooled to room temperature presented by the blue solid line. The black line represents the intensities of the sample heated up to 780 °C, where the sample is decomposed. (b) DSC measurement result of OIL-type LTTO. (c) In situ variant-temperature PXD pattern of γ -LTTO upon heating. The data after measurements are placed on the top for comparison. Blue lines represent the γ -phase; gray lines represent mixed phases; purple lines represent the α -phase. (d) Temperature-dependent evolution of the lattice parameters of LTTO. The blue region represents the γ -phase; the white region represents mixed phases; and the purple region represents the α -phase. The red symbols represent the cell parameters of the α -phase cooled down to room temperature.

(thermodynamically stable phase)⁴⁹ and can be synthesized by the conventional solid-state reaction at ambient pressure.⁵⁰ The energy of the β -phase (NTO-type R3) becomes lower than that of the α -phase above 6 GPa as has been experimentally validated in our previous work.³⁷ As the volume becomes smaller than 82 Å³/formula unit, P21/n is the most stable phase, suggesting that β -phase will further transform to a perovskite P21/n structure (hereafter denoted as δ -phase) above ~40 GPa. In contrast, γ -phase (OIL-type R3) with the largest V_0 (111.5 Å³/formula unit) is metastable all the way from its V_0 down to the minimum volume within our calculation range, which means this metastable phase cannot be obtained by high-pressure synthesis. Figure 3b indicates that the γ -phase becomes more stable than the α -one upon volumetric expansion, namely, the γ -phase may be stabilized under “negative pressure”, which can only be achieved by chemical methods, such as solid solution, interfacial strain, or ionic exchange in this work, initiated by lattice mismatch. When it comes to the pressure effect on the volume of a lattice, “negative pressure” brings volumetric expansion. In this work, the calculated equilibrium volume of NTTO is around 129.80 Å³/formula (Figure 3a), which locates at the “negative pressure” range in Figure 3b, where the R3-OIL structure is more stable than the Pnn2 polymorph. In other words, the larger ionic radius of Na⁺ than that of Li⁺ as well as the resulting expanded cell volume introduces “negative pressure” into the lattice and thus stabilizes the R3-OIL structure. Then, via a low-temperature topotactic ion-exchange reaction, the “negative pressure” is driven to transfer from NTTO to the

LTTO lattice and the R3-OIL structure is preserved during the substitution of Na⁺ by Li⁺. To quantify the “negative pressure”, we constructed the P–V relation using the parameters obtained from Murnaghan EOS fitting of the E–V curve of the α -phase so that the corresponding pressure of each volume could be read at the top axis in Figure 3b. Here, γ -LTTO is intercepted as a metastable phase under ambient pressure by a more facile chemical method, inducing a negative chemical pressure of around -6 GPa based on the P–V relation of the α -phase regarding the energy-crossover volume of Pnn2 and R3-OIL.

Thus far, there are four polymorphs of LTTO, namely, the thermodynamically stable α -phase (Pnn2, Figure S5a),⁵⁰ the metastable β -phase (NTO-type R3) quenched from high-temperature and high-pressure synthesis (Figure S5b),³⁷ and the new γ -LTTO (OIL-type R3) obtained from the low-temperature topotactic reaction in this work (the inset of Figure 2b). The fourth predicted δ -LTTO (P21/n) phase has not been experimentally prepared yet and needs further investigation. The equilibrium volumes of LTTO decrease successively in the order of γ , α , β , and δ -LTTO. A similar volume–polymorph evolution trend has also been observed in NTTO (Figure 3a) and other Li₂BB'O₆ compounds;³⁷ to the best of our knowledge, this seems a common rule of equilibrium volumes of different polymorphs for nonmagnetic exotic perovskite-related compounds. The polymorph transitions of LTTO and NTTO are schematically exhibited in Figure 3c. Theoretically, the high-pressure phase favors higher density as observed in LTTO. The calculated density of LTTO

increases from 3.95 g/cm³ for the γ -phase to 4.39, 4.94, and 5.93 g/cm³ for the α -, β -, and δ -polymorphs, respectively. These findings clearly show that if the volume/formula unit of a metastable polymorph is smaller than that of a stable phase, then it could be possibly stabilized by high-pressure synthesis. Otherwise, the metastable phase should only be intercepted by chemically induced “negative pressure” (volumetric expansion). Thereby, chemical interception like topotactic reaction is an excellent and complementing way to approach a metastable phase for solid-state functional materials to realize practical applications.

Temperature-Dependent SHG Evolution. Thermodynamically, the metastable phases can either convert to their ground-state counterparts or decompose upon heating at ambient pressure. Similarly, most acentric materials can go through a reversible second-order phase transition to centrosymmetric structures at a higher temperature,^{51–54} except that some monolayer 2D transition-metal dichalcogenides⁵⁵ and RbNaMgP₂O₇^{56,57} prefer to transform to other acentric structures via ionic displacement and exhibit enhanced SHG intensity upon heating because of their unique structural features. In contrast, the SHG intensity of most 3D structural materials tends to be faded in the elevated temperature range. As far as we know, we present here for the first time the intensive increase of SHG intensity of γ -LTTO at a higher temperature. The *in situ* variant-temperature SHG activity of γ -LTTO is shown in Figure 4a. The SHG intensity drastically increases around 560 °C and reaches the maximum value of about 500 times the initial intensity (red solid line) around 620 °C, after which the high SHG intensity is somehow slightly intensified upon cooling to room temperature (blue solid line). The drastic increase of SHG intensity around 560 °C is attributed to an irreversible first-order structural transition from the γ -phase to the thermodynamically stable α -phase maintained down to room temperature, which is confirmed by the PXD measurement (Figure S6) of the SHG sample cooled from 680 °C (Figure 4a), in good accordance with the reported high SHG intensity of α -LTTO.⁵⁸ The DSC measurement in Figure 4b exhibits a sharp exothermal peak around 650 °C, signaling a first-order structural transition to a more stable phase. We also performed *in situ* variant-temperature PXD measurements for γ -LTTO at elevated temperatures up to 760 °C and then cooled down to room temperature. PXD patterns at different temperatures are piled up for comparison in Figure 4c. γ -LTTO was retained up to 580 °C with diffraction peaks slightly moving to lower angles, indicating lattice expansion as shown in the blue region in Figure 4d. A secondary phase emerges at 600 °C and coexists with γ -LTTO until 620 °C (the white region in Figure 4d). Above 620 °C, γ -LTTO completely transforms to the secondary phase identified as α -LTTO (*Pnn2*) (the purple region in Figure 4d), which echoes the drastic increase of the SHG signal in Figure 4a. When cooled down to room temperature, the α -phase was maintained from high temperatures with decreased lattice parameters (red symbols in Figure 4d). Furthermore, when the sample was further heated to temperatures higher than 780 °C, α -LTTO starts to decompose. The PXD pattern of the sample cooled from 780 °C (Figure S6) identifies the remains as a mixture of decomposed centrosymmetric compounds and a small fraction of α -LTTO, which well explains the sharp drop of SHG intensity over 700 °C.

The above findings indicate that γ -LTTO can be used to construct SHG-response-based irreversible temperature sensors. On one hand, irreversible optical temperature sensors have been developed to record temperatures at extreme conditions, such as detonation events,^{59,60} and readout the historic temperatures at ambient conditions, which avoids the impact of blackbody radiation at high temperatures and reduces the cost of building *in situ* probing device.^{61–63} On the other hand, SHG is a polarization process, in which two photons are converted to one photon of double frequency, and does not include real adsorption. Thus, it greatly reduces photobleaching or other photodamage phenomena.⁶⁴ Remarkably, thanks to the large difference of SHG intensities of the “on” and “off” states in γ -LTTO, this material could be utilized with a very small amount (a few micrograms) to be integrated into arrays and image the spatial temperature distribution.⁶¹

CONCLUSIONS

In summary, we synthesized a new metastable phase of Li₂TiTeO₆ in the OIL-type *R3* structure via a low-temperature topotactic ion exchange from Na₂TiTeO₆. Revisiting of Na₂TiTeO₆ revealed its acentric OIL-type *R3* structure instead of the reported *R*₃ phase. The novel metastable OIL-type γ -Li₂TiTeO₆ undergoes an irreversible first-order phase transition to the α -phase (*Pnn2*) at temperatures over 560 °C, accompanied by a steep intensity increase of SHG intensity. At a higher temperature, γ -Li₂TiTeO₆ starts to decompose. γ -Li₂TiTeO₆ could be utilized as SHG-based disposal high-temperature recorder because of its giant SHG intensity switching. DFT calculations reveal that γ -Li₂TiTeO₆ is thermodynamically favored over the stable α -Li₂TiTeO₆ at negative chemical pressures around -6 GPa and perovskite-type δ -Li₂TiTeO₆ can be formed around 40 GPa. These findings indicate that topotactic chemical interception is a promising and excellent approach to explore metastable phases and intriguing properties.

ASSOCIATED CONTENT

Supporting Information

The Supporting Information is available free of charge at <https://pubs.acs.org/doi/10.1021/acs.chemmater.2c02957>.

Crystallographic details of NTTO-OIL and NTTO-ilmenite (Table S1); crystallographic details of α -, β -, γ -, and δ -LTTO (Table S2); a schematic of the device configuration for temperature-dependent SHG measurement (Figure S1); PXD patterns of NTTO and LTTO in various polymorphs (Figure S2); elemental analysis results of NTTO-OIL and γ -LTTO (Figure S3); Rietveld refinement results of NTTO-ilmenite (Figure S4); crystal structures of α - and β -LTTO (Figure S5); PXD patterns of products retained from high-temperature SHG measurements up to 680 and 780 °C (Figure S6);

crystallographic information files for OIL-type Na₂TiTeO₆ and γ -Li₂TiTeO₆ (PDF)

Accession Codes

The supporting crystallographic information files may also be obtained from FIZ Karlsruhe, 76344 Eggenstein-Leopoldshafen, Germany (email: crysdata@fiz-karlsruhe.de), on quoting the deposition number CSD-2193645 (NTTO) and CSD-2193646 (γ -LTTO).

AUTHOR INFORMATION

Corresponding Authors

Yonggang Wang – School of Materials Science and Engineering, Peking University, Beijing 100871, China;  orcid.org/0000-0003-4816-9182; Email: ygw@pku.edu.cn

Man-Rong Li – Key Laboratory of Bioinorganic and Synthetic Chemistry of Ministry of Education, School of Chemistry, Sun Yat-Sen University, Guangzhou 510006, China;  orcid.org/0000-0001-8424-9134; Email: limanrong@mail.sysu.edu.cn

Authors

Mei-Huan Zhao – Key Laboratory of Bioinorganic and Synthetic Chemistry of Ministry of Education, School of Chemistry, Sun Yat-Sen University, Guangzhou 510006, China;  orcid.org/0000-0002-3676-3259

Xiao Zhou – Key Laboratory of Bioinorganic and Synthetic Chemistry of Ministry of Education, School of Chemistry, Sun Yat-Sen University, Guangzhou 510006, China

Yifeng Han – Key Laboratory of Bioinorganic and Synthetic Chemistry of Ministry of Education, School of Chemistry, Sun Yat-Sen University, Guangzhou 510006, China

Dequan Jiang – School of Materials Science and Engineering, Peking University, Beijing 100871, China

Kuo Li – Center for High Pressure Science and Technology Advanced Research (HPSTAR), Beijing 100094, China;  orcid.org/0000-0002-4859-6099

Haiyan Zheng – Center for High Pressure Science and Technology Advanced Research (HPSTAR), Beijing 100094, China;  orcid.org/0000-0002-4727-5912

Huiyang Gou – Center for High Pressure Science and Technology Advanced Research (HPSTAR), Beijing 100094, China

Ling Chen – Beijing Key Laboratory of Energy Conversion and Storage Materials, College of Chemistry, Beijing Normal University, Beijing 100875, China;  orcid.org/0000-0002-3693-4193

Complete contact information is available at:

<https://pubs.acs.org/10.1021/acs.chemmater.2c02957>

Notes

The authors declare no competing financial interest.

ACKNOWLEDGMENTS

This work was financially supported by the National Natural Science Foundation of China (NSFC-22090041 and NSFC-21875287) and the Program for Guangdong Introducing Innovative and Entrepreneurial Teams (2017ZT07C069). The authors thank beamline BL14B1 (SSRF) for providing the beam time and the National Supercomputer Center in Guangzhou.

REFERENCES

- (1) Brus, L. Metastable DenseSemiconductor phases. *Science* **1997**, *276*, 373–374.
- (2) Badding, J. V. High-pressure synthesis, characterization, and tuning of solid state materials. *Annu. Rev. Mater. Sci.* **1998**, *28*, 631–658.
- (3) Su, Y.; Tsujimoto, Y.; Matsushita, Y.; Yuan, Y.; He, J.; Yamaura, K. High-pressure synthesis, crystal structure, and magnetic properties of $\text{Sr}_2\text{MnO}_3\text{F}$: A new member of layered perovskite oxyfluorides. *Inorg. Chem.* **2016**, *55*, 2627–2633.
- (4) Gainza, J.; Serrano-Sánchez, F.; Rodrigues, J. E. F. S.; Nemes, N. M.; Martínez, J. L.; Alonso, J. A. Metastable materials accessed under moderate pressure conditions ($P \leq 3.5$ GPa) in a piston-cylinder press. *Materials* **2021**, *14*, 1946.
- (5) Zhang, W.; Oganov Artem, R.; Goncharov Alexander, F.; Zhu, Q.; Boulfelfel Salah, E.; Lyakhov Andriy, O.; Stavrou, E.; Somayazulu, M.; Prakapenka Vitali, B.; Konôpková, Z. Unexpected stable stoichiometries of sodium chlorides. *Science* **2013**, *342*, 1502–1505.
- (6) Fukuda, M.; Yamada, I.; Murata, H.; Hojo, H.; Hernandez, O. J.; Ritter, C.; Tanaka, K.; Fujita, K. Perovskite-type CuNbO_3 exhibiting unusual noncollinear ferrielectric to collinear ferroelectric dipole order transition. *Chem. Mater.* **2020**, *32*, 5016–5027.
- (7) Lin, K.; Li, Q.; Yu, R.; Chen, J.; Attfield, J. P.; Xing, X. Chemical pressure in functional materials. *Chem. Soc. Rev.* **2022**, *51*, 5351–5364.
- (8) Han, Y.; Zhu, C.; Peng, Y.; Li, S.; Wu, M.; Zhao, S.; Deng, Z.; Jin, C.; Du, W.; Walker, D.; Li, M.-R. Above-room-temperature LiNbO_3 -type polar magnet stabilized by chemical and physical pressure. *Chem. Mater.* **2020**, *32*, 1618–1626.
- (9) Liu, S.; He, L.; Wang, Y.; Shi, P.; Ye, Q. Tunable phase transition, band gap and SHG properties by halogen replacement of hybrid perovskites [(thiomorpholinium) PbX_3 , $X = \text{Cl}, \text{Br}, \text{I}$]. *Chin. Chem. Lett.* **2022**, *33*, 1032–1036.
- (10) Li, L.; Huang, F.; Shi, Y.; Luo, Z.-Z.; Wang, G.-Q.; Li, X.-X.; Li, B.; Zhang, L.; Yu, Y.; Feng, Y.-N.; Yang, C.; Yu, Y.; Poeppelmeier, K. R. Triple-wavelength lasing with a stabilized β -LaBSiOS:Nd³⁺ crystal. *J. Am. Chem. Soc.* **2022**, *144*, 11822–11830.
- (11) Jackel, J. L.; Rice, C. E. Topotactic LiNbO_3 to cubic perovskite structural transformation in LiNbO_3 and LiTaO_3 . *Ferroelectrics* **1981**, *38*, 801–804.
- (12) Jeen, H.; Choi, W. S.; Freeland, J. W.; Ohta, H.; Jung, C. U.; Lee, H. N. Topotactic phase transformation of the brownmillerite $\text{SrCo}_{2.5}$ to the perovskite $\text{SrCoO}_{3-\delta}$. *Adv. Mater.* **2013**, *25*, 3651–3656.
- (13) Hyett, G.; Barrier, N.; Clarke, S. J.; Hadermann, J. Topotactic oxidative and reductive control of the structures and properties of layered manganese oxychalcogenides. *J. Am. Chem. Soc.* **2007**, *129*, 11192–11201.
- (14) Li, M.-R.; Adem, U.; McMitchell, S. R. C.; Xu, Z.; Thomas, C. I.; Warren, J. E.; Giap, D. V.; Niu, H.; Wan, X.; Palgrave, R. G.; Schiffmann, F.; Cora, F.; Slater, B.; Burnett, T. L.; Cain, M. G.; Abakumov, A. M.; van Tendeloo, G.; Thomas, M. F.; Rosseinsky, M. J.; Claridge, J. B. A polar corundum oxide displaying weak ferromagnetism at room temperature. *J. Am. Chem. Soc.* **2012**, *134*, 3737–3747.
- (15) Wang, Y.; Zhang, L.; Wang, J.; Li, Q.; Wang, H.; Gu, L.; Chen, J.; Deng, J.; Lin, K.; Huang, L.; Xing, X. Chemical-pressure-modulated BaTiO_3 thin films with large spontaneous polarization and high curie temperature. *J. Am. Chem. Soc.* **2021**, *143*, 6491–6497.
- (16) Zhang, L.; Chen, J.; Fan, L.; Diéguez, O.; Cao, J.; Pan, Z.; Wang, Y.; Wang, J.; Kim, M.; Deng, S.; Wang, J.; Wang, H.; Deng, J.; Yu, R.; Scott, J. F.; Xing, X. Giant polarization in super-tetragonal thin films through interphase strain. *Science* **2018**, *361*, 494.
- (17) McHale, J. M.; Auroux, A.; Perrotta, A. J.; Navrotsky, A. Surface energies and thermodynamic phase stability in nanocrystalline aluminas. *Science* **1997**, *277*, 788.
- (18) Navrotsky, A. Energetic clues to pathways to biominerilization: precursors, clusters, and nanoparticles. *Proc. Natl. Acad. Sci. U.S.A.* **2004**, *101*, 12096.
- (19) Sakurai, S.; Namai, A.; Hashimoto, K.; Ohkoshi, S.-I. First observation of phase transformation of all four Fe_2O_3 phases ($\gamma \rightarrow \epsilon \rightarrow \beta \rightarrow \alpha$ -phase). *J. Am. Chem. Soc.* **2009**, *131*, 18299–18303.
- (20) Gurlo, A. Structural stability of high-pressure polymorphs in In_2O_3 nanocrystals: Evidence of stress-induced transition? *Angew. Chem., Int. Ed.* **2010**, *49*, 5610–5612.
- (21) Zhao, S.; Yang, J.; Han, Y.; Wu, M.; Li, M.-R. Modulation of ionic arrangement in polar magnet by chemical pressure. *Chin. Chem. Lett.* **2022**, DOI: [10.1016/j.cclet.2022.03.078](https://doi.org/10.1016/j.cclet.2022.03.078).

- (22) Qasim, I.; Kennedy, B. J.; Avdeev, M. Stabilising the orthorhombic perovskite structure in SrIrO_3 through chemical doping. Synthesis, structure and magnetic properties of $\text{SrIr}_{1-x}\text{Mg}_x\text{O}_3$ ($0.20 \leq x \leq 0.33$). *J. Mater. Chem. A* **2013**, *1*, 13357–13362.
- (23) Amano Patino, M.; Smith, T.; Zhang, W.; Halasyamani, P. S.; Hayward, M. A. Cation exchange in a 3D perovskite-synthesis of $\text{Ni}_{0.5}\text{TaO}_3$. *Inorg. Chem.* **2014**, *53*, 8020–8024.
- (24) Meena, V.; Mandal, T. K. Topotactic ion exchange in a three-dimensional close-packed trirutile structure with an octahedral network. *Inorg. Chem.* **2019**, *58*, 2921–2924.
- (25) Schaak, R. E.; Mallouk, T. E. Perovskites by design: A toolbox of solid-state reactions. *Chem. Mater.* **2002**, *14*, 1455–1471.
- (26) Sanjaya Ranmohotti, K. G.; Josepha, E.; Choi, J.; Zhang, J.; Wiley, J. B. Topochemical manipulation of perovskites: Low-temperature reaction strategies for directing structure and properties. *Adv. Mater.* **2011**, *23*, 442–460.
- (27) Schaak, R. E.; Mallouk, T. E. Topochemical synthesis of three-dimensional perovskites from lamellar precursors. *J. Am. Chem. Soc.* **2000**, *122*, 2798–2803.
- (28) Josepha, E. A.; Farooq, S.; Mitchell, C. M.; Wiley, J. B. Synthesis and thermal stability studies of a series of metastable Dion–Jacobson double-layered neodymium-niobate perovskites. *J. Solid State Chem.* **2014**, *216*, 85–90.
- (29) Hermann, A. T.; Wiley, J. B. Thermal stability of Dion–Jacobson mixed-metal-niobate double-layered perovskites. *Mater. Res. Bull.* **2009**, *44*, 1046–1050.
- (30) Nalbandyan, V. B.; Avdeev, M.; Pospelov, A. A. Ion exchange reactions of NaSbO_3 and morphotropic series MSbO_3 . *Solid State Sci.* **2006**, *8*, 1430–1437.
- (31) Inaguma, Y.; Aimi, A.; Mori, D.; Katsumata, T.; Ohtake, M.; Nakayama, M.; Yonemura, M. High-pressure synthesis, crystal structure, chemical bonding, and ferroelectricity of LiNbO_3 -type LiSbO_3 . *Inorg. Chem.* **2018**, *57*, 15462–15473.
- (32) Shao, Z.; Saitzek, S.; Ferri, A.; Riquit, M.; Dupont, L.; Roussel, P.; Desfeux, R. Evidence of ferroelectricity in metastable $\text{Sm}_2\text{Ti}_2\text{O}_7$ thin film. *J. Mater. Chem.* **2012**, *22*, 9806–9812.
- (33) Hamasaki, Y.; Shimizu, T.; Yasui, S.; Taniyama, T.; Sakata, O.; Itoh, M. Crystal isomers of ScFeO_3 . *Cryst. Growth Des.* **2016**, *16*, 5214–5222.
- (34) Zhao, R.; Yang, C.; Wang, H.; Jiang, K.; Wu, H.; Shen, S.; Wang, L.; Sun, Y.; Jin, K.; Gao, J.; Chen, L.; Wang, H.; MacManus-Driscoll, J. L.; van Aken, P. A.; Hong, J.; Li, W.; Yang, H. Emergent multiferroism with magnetodielectric coupling in EuTiO_3 created by a negative pressure control of strong spin-phonon coupling. *Nat. Commun.* **2022**, *13*, No. 2364.
- (35) Barnard, A. S.; Zapol, P. Effects of particle morphology and surface hydrogenation on the phase stability of TiO_2 . *Phys. Rev. B* **2004**, *70*, No. 235403.
- (36) Farvid, S. S.; Dave, N.; Radovanovic, P. V. Phase-controlled synthesis of colloidal In_2O_3 nanocrystals via size-structure correlation. *Chem. Mater.* **2010**, *22*, 9–11.
- (37) Zhao, M.-H.; Zhu, C.; Sun, Z.; Xia, T.; Han, Y.; Zeng, Y.; Gao, Z.; Gong, Y.; Wang, X.; Hong, J.; Zhang, W.-X.; Wang, Y.; Yao, D.-X.; Li, M.-R. Methodological approach to the high-pressure synthesis of nonmagnetic $\text{Li}_2\text{B}^{4+}\text{B}^{6+}\text{O}_6$ oxides. *Chem. Mater.* **2022**, *34*, 186–196.
- (38) Park, J. H.; Parise, J. B.; Woodward, P. M.; Lubomirsky, I.; Stafsudd, O. A novel approach for identifying and synthesizing high dielectric materials. *J. Mater. Res.* **1999**, *14*, 3192–3195.
- (39) Coelho, A. A. TOPAS and TOPAS-Academic: An optimization program integrating computer algebra and crystallographic objects written in C++. *J. Appl. Crystallogr.* **2018**, *51*, 210–218.
- (40) Kresse, G.; Joubert, D. From ultrasoft pseudopotentials to the projector augmented-wave method. *Phys. Rev. B* **1999**, *59*, 1758–1775.
- (41) Perdew, J. P.; Burke, K.; Ernzerhof, M. Generalized gradient approximation made simple. *Phys. Rev. Lett.* **1996**, *77*, 3865–3868.
- (42) Murnaghan, F. D. The compressibility of media under extreme pressures. *Proc. Natl. Acad. Sci. U.S.A.* **1944**, *30*, 244–247.
- (43) Woodward, P. M.; Sleight, A. W.; Du, L.-S.; Grey, C. P. Structural studies and order-disorder phenomenon in a series of new quaternary tellurates of the type $A^{2+}\text{M}^{4+}\text{Te}^{6+}\text{O}_6$ and $A^{1+2}\text{M}^{4+}\text{Te}^{6+}\text{O}_6$. *J. Solid State Chem.* **1999**, *147*, 99–116.
- (44) Zhao, M.-H.; Wang, W.; Han, Y.; Xu, X.; Sheng, Z.; Wang, Y.; Wu, M.; Grams, C. P.; Hemberger, J.; Walker, D.; Greenblatt, M.; Li, M.-R. Reversible structural transformation between polar polymorphs of $\text{Li}_2\text{GeTeO}_6$. *Inorg. Chem.* **2019**, *58*, 1599–1606.
- (45) Arévalo-López, Á. M.; Solana-Madruga, E.; Arévalo-López, E. P.; Khalyavin, D.; Kepa, M.; Dos santos-García, A. J.; Sáez-Puche, R.; Attfield, J. P. Evolving spin periodicity and lock-in transition in the frustrated ordered ilmenite-type $\beta-\text{Mn}_2\text{InSbO}_6$. *Phys. Rev. B* **2018**, *98*, No. 214403.
- (46) Solana-Madruga, E.; Ritter, C.; Mentré, O.; Attfield, J. P.; Arévalo-López, Á. M. Giant coercivity and spin clusters in high pressure polymorphs of $\text{Mn}_2\text{LiReO}_6$. *J. Mater. Chem. C* **2022**, *10*, 4336–4341.
- (47) Li, M.-R.; Retuerto, M.; Stephens, P. W.; Croft, M.; Sheptyakov, D.; Pomjakushin, V.; Deng, Z.; Akamatsu, H.; Gopalan, V.; Sánchez-Benítez, J.; Saouma, F. O.; Jang, J. I.; Walker, D.; Greenblatt, M. Low-temperature cationic rearrangement in a bulk metal oxide. *Angew. Chem., Int. Ed.* **2016**, *55*, 9862–9867.
- (48) Shannon, R. D. Revised effective ionic radii and systematic studies of interatomic distances in halides and chalcogenides. *Acta Crystallogr., Sect. A: Cryst. Phys., Diff., Theor. Gen. Crystallogr.* **1976**, *32*, 751–767.
- (49) Sun, W.; Dacek, S. T.; Ong, S. P.; Hautier, G.; Jain, A.; Richards, W. D.; Gamst, A. C.; Persson, K. A.; Ceder, G. The thermodynamic scale of inorganic crystalline metastability. *Sci. Adv.* **2016**, *2*, No. e1600225.
- (50) Choisnet, J.; Rulmont, A.; Tarte, P. Ordering phenomena in the LiSbO_3 type structure: The new mixed tellurates $\text{Li}_2\text{TiTeO}_6$ and $\text{Li}_2\text{SnTeO}_6$. *J. Solid State Chem.* **1989**, *82*, 272–278.
- (51) Wang, D.; Zhang, Y.; Shi, Q.; Liu, Q.; Yang, D.; Zhang, B.; Wang, Y. Tellurate polymorphs with high-performance nonlinear optical switch property and wide mid-IR transparency. *Inorg. Chem. Front.* **2022**, *9*, 1708–1713.
- (52) Wakita, K.; Hagiwara, M.; Paucar, R.; Shim, Y.; Mimura, K.; Mamedov, N. Evaluation of crystal structure in TlInS_2 by optical second-harmonic generation. *J. Phys. Conf. Ser.* **2015**, *619*, No. 012006.
- (53) Xiong, R.-G. The temperature-dependent domains, SHG effect and piezoelectric coefficient of TGS. *Chin. Chem. Lett.* **2013**, *24*, 681–684.
- (54) Cai, H.-L.; Zhang, W.; Ge, J.-Z.; Zhang, Y.; Awaga, K.; Nakamura, T.; Xiong, R.-G. 4-(cyanomethyl)anilinium perchlorate: A new displacive-type molecular ferroelectric. *Phys. Rev. Lett.* **2011**, *107*, No. 147601.
- (55) Khan, A. R.; Liu, B.; Zhang, L.; Zhu, Y.; He, X.; Zhang, L.; Lü, T.; Lu, Y. Extraordinary temperature dependent second harmonic generation in atomically thin layers of transition-metal dichalcogenides. *Adv. Opt. Mater.* **2020**, *8*, No. 2000441.
- (56) Zhao, S.; Yang, X.; Yang, Y.; Kuang, X.; Lu, F.; Shan, P.; Sun, Z.; Lin, Z.; Hong, M.; Luo, J. Non-centrosymmetric $\text{RbNaMgP}_2\text{O}_7$ with unprecedented thermo-induced enhancement of second harmonic generation. *J. Am. Chem. Soc.* **2018**, *140*, 1592–1595.
- (57) Yang, X.; Zhao, S.; Geng, S.; Yang, L.; Huang, Q.; Kuang, X.; Luo, J.; Xing, X. Structural origin of thermally induced second harmonic generation enhancement in $\text{RbNaMgP}_2\text{O}_7$. *Chem. Mater.* **2019**, *31*, 9843–9849.
- (58) Du, X.; Guo, X.; Gao, Z.; Liu, F.; Guo, F.; Wang, S.; Wang, H.; Sun, Y.; Tao, X. Li_2MTeO_6 ($\text{M} = \text{Ti}, \text{Sn}$): Mid-infrared nonlinear optical crystal with strong second harmonic generation response and wide transparency range. *Angew. Chem., Int. Ed.* **2021**, *60*, 23320–23326.
- (59) Sun, H.; Yu, M.; Sun, X.; Wang, G.; Lian, J. Effective temperature sensing by irreversible morphology evolution of ultrathin gold island films. *J. Phys. Chem. C* **2013**, *117*, 3366–3373.

- (60) Sudheer; Mondal, P.; Rai, V. N.; Srivastava, A. K. A study of growth and thermal dewetting behavior of ultra-thin gold films using transmission electron microscopy. *AIP Adv.* **2017**, *7*, No. 075303.
- (61) Khalid, A.; Kontis, K. Thermographic phosphors for high temperature measurements: Principles, current state of the art and recent applications. *Sensors* **2008**, *8*, 5673–5744.
- (62) Salek, G.; Demourgues, A.; Jubera, V.; Garcia, A.; Gaudon, M. Mn²⁺ doped Zn₃(PO₄)₂ phosphors: Irreversible thermochromic materials useful as thermal sensors. *Opt. Mater.* **2015**, *47*, 323–327.
- (63) Salek, G.; Devoti, A.; Lataste, E.; Demourgues, A.; Garcia, A.; Jubera, V.; Gaudon, M. Optical properties versus temperature of Cr-doped γ - and α -Al₂O₃: Irreversible thermal sensors application. *J. Lumin.* **2016**, *179*, 189–196.
- (64) Zheng, T.; Runowski, M.; Martín, I. R.; Lis, S.; Vega, M.; Llanos, J. Nonlinear optical thermometry—a novel temperature sensing strategy via second harmonic generation (SHG) and upconversion luminescence in BaTiO₃: Ho³⁺, Yb³⁺ perovskite. *Adv. Opt. Mater.* **2021**, *9*, No. 2100386.

□ Recommended by ACS

Cation and Lone Pair Order–Disorder in the Polymorphic Mixed Metal Bismuth Scheelite Bi_xFeMo₃O₁₂

Matilde Saura-Múzquiz, Brendan J. Kennedy, *et al.*

DECEMBER 23, 2022

CHEMISTRY OF MATERIALS

READ ▶

Method to Determine the Distribution of Substituted or Intercalated Ions in Transition-Metal Dichalcogenides: Fe_xVSe₂ and Fe_{1-x}V_xSe₂

Mellie Lemon, David C. Johnson, *et al.*

SEPTEMBER 28, 2022

CHEMISTRY OF MATERIALS

READ ▶

Synthesis, Crystal Structures, Mechanical Properties, and Formation Mechanisms of Cubic Tungsten Nitrides

Xuefeng Zhou, Shanmin Wang, *et al.*

OCTOBER 11, 2022

CHEMISTRY OF MATERIALS

READ ▶

Synthesis and Calculations of Wurtzite Al_{1-x}Gd_xN Heterostructural Alloys

Rebecca W. Smaha, Nancy M. Haegel, *et al.*

NOVEMBER 21, 2022

CHEMISTRY OF MATERIALS

READ ▶

Get More Suggestions >